Surface-confined self-reconstruction to sulfate-terminated ultrathin layers on NiMo$_3$S$_4$ toward biomass molecule electro-oxidation

Tong Wu [a,b,1], Zian Xu [c,d,1], Xunlu Wang [a,1], Mengjia Luo [a,b], Yu Xia [c], Xingcai Zhang [e], Jiantao Li [f], Jie Liu [a], Jiacheng Wang [a,b,h,*], Hsing-Lin Wang [c,**], Fuqiang Huang [a,b,g,*]

[a] State Key Laboratory of High Performance Ceramics and Superfine Microstructure, Shanghai Institute of Ceramics, Chinese Academy of Sciences, Shanghai 200050, China
[b] Center of Materials Science and Optoelectronics Engineering, University of Chinese Academy of Sciences, Beijing 100049, China
[c] Department of Materials Science and Engineering, Southern University of Science and Technology, Shenzhen 518055, Guangdong Province, China
[d] Institute of Applied Physics and Materials Engineering, University of Macau, Macao Special Administrative Region of China
[e] John A. Paulson School of Engineering and Applied Sciences, Harvard University, Cambridge, MA 02138, USA
[f] State Key Laboratory of Advanced Technology for Materials Synthesis and processing, Wuhan University of Technology, Wuhan 430070, Hubei, China
[g] State Key Laboratory of Rare Earth Materials Chemistry and Applications, College of Chemistry and Molecular Engineering, Peking University, Beijing 100871, China
[h] School of Materials Science and Engineering, Taizhou University, Taizhou 318000, China

ARTICLE INFO

ABSTRACT

Developing high-performance anode electrocatalysts is desirable in electrocatalytic energy devices powered by sustainable electricity. Compared to water oxidation using Ni-based anodes, electro-oxidation upgrading of biomass molecule with larger size lacks dynamics driving due to increased thickness and decreased electron transfer kinetics of insulating NiOOH amorphous layer (>50 nm) from uncontrollable in-depth reconstruction. Herein, a self-confined surface reconstruction strategy is proposed to construct ~5 nm-thick NiOOH layers on NiMo$_3$S$_4$ with superior activity and stability for 5-hydroxymethylfurfural oxidation reaction (HMFOR). *In-situ* high-valence Mo-O coordination and sulfate-terminated anion groups effectively prevent in-depth surface oxidation, leading to the ultra-thin active layers with increased electron transfer kinetics. The surface self-reconstructed NiMo$_3$S$_4$ (NiMo$_3$S$_4$-R) exhibits nearly 100% of HMF conversion, FDCA selectivity and Faradaic efficiency, much better than sulfate-modified NiOOH and pure NiOOH. Moreover, a paired electrolyzer of NiMo$_3$S$_4$-R||NiMo$_3$S$_4$ for HMFOR||HER is also assembled with an ultralow voltage of 1.414 V at 10 mA cm^{-2}.

1. Introduction

With the rapid consumption of fossil fuels and the resulting pollution, the development of clean and renewable energy is particularly important. To achieve sustainable production of hydrogen, electrochemical water splitting is one of the most promising strategies [1]. However, the high energy consumption required for hydrogen production is due to the sluggish oxygen evolution reaction (OER). Additionally, taking into account the low value of O$_2$ produced by the OER, substituting biomass oxidation for the sluggish OER can significantly reduce the overpotential while obtaining high-value chemicals [2,3]. 5-Hydroxymethylfurfural (HMF) is an important biochemical substance

that is produced by dehydration of cellulose biomass, which is used as a precursor of fine chemicals and can be selectively oxidized to pharmaceuticals and monomers [4]. For example, 2,5-furandicarboxylic acid (FDCA) is an important green chemical monomer synthesized by direct oxidation of HMF, which can replace petroleum-derived polyethylene terephthalate to prepare poly(ethylene 2,5-furandicarboxylate) and can be used to prepare renewable bioplastics to replace petroleum-based monomeric terephthalic acid [5]. Therefore, combining the HMF oxidation reaction (HMFOR) with the hydrogen evolution reaction (HER) enables the synthesis of high value-added products as well as the efficient production of hydrogen.

Due to the high costs of noble metals electrocatalysts toward HMFOR

in alkaline electrolytes [6,7], it is very important to develop low-cost and high-performance electrocatalysts through rational design [8–10]. In recent years, transition metal catalysts (Ni, Co, Fe, and Mo-based compounds, *etc.*) have shown excellent activities for the OER and HMFOR [11–16]. For the OER, transition metal catalysts, especially Ni-based compounds, are precursors of active substances, while the true active substances most likely take the form of oxyhydroxide [17–20]. Recent works have adapted the strategy to optimize the OER a-ctivity of oxyhydroxide by single metal doped or (oxo)anion adsorption regulation, such as Fe, Cu, sulfate, molybdate, and phosphate anions [21–27]. For example, the irreversible phase transformation from nickel-based pnictide/sulfide materials to NiOOH demonstrate NiOOH as the key active species for OER [28]. Moreover, the etching-leaching-reconstruction engineering to achieve complete reconstruction of $NiMoO_4 \cdot xH_2O$, which consists of complete collapse of hydrates with co-leaching of crystal water and MoO_4^{2-} and then its reconstruction to NiOOH via electro-oxidation [29]. However, the thickness regulation of oxyhydroxide layer plays an important role in water electrolysis performance [30–33]. A few oxyhydroxide layer (<3 nm) could accelerate the charge transfer for water oxidation, while it suffers from poor stability. A thick oxyhydroxide layer (50–100 nm) could protect the electrode, but it results in a reduced conductivity. The optimal ultrathin oxyhydroxide layer at about 5–10 nm can effectively promote charge transfer without affecting the stability. It has been reported that effective electron donor substitution into 2D nanostructures can form unique surface dipoles, which can not only stabilize metastable surface structures but also provide higher chemical reactivity [34,35]. However, much remains unknown about the in situ self-reconstruction strategy to prepare optimal ultrathin oxyhydroxide layer with enhanced stability and activity toward chemical upgrading.

Herein, we developed a surface-confined self-reconstruction strategy of constructing an ultrathin (Ni, Mo)OOH layer (~5 nm) with sulfate-terminated species via electrochemical activation of $NiMo_3S_4$ in 1 M KOH, boosting the 5-hydroxymethylfurfural oxidation reaction (HMFOR). The initial electrochemical activation process leads to the extraction of Mo and S atoms on the surface of $NiMo_3S_4$. Then the subsequent activation could result in the self-modifying of Mo atoms and sulfate oxoanions into the framework of NiOOH, thus forming ultrathin (Ni, Mo)OOH layer with sulfate-terminated species on $NiMo_3S_4$ while maintaining the bulk crystalline structure of $NiMo_3S_4$. The atomic layer thickness of (Ni, Mo)OOH is guided by the terminated groups of sulfate to prevent surface overoxidation of $NiMo_3S_4$, and the Mo atoms partially substitute the Ni site of NiOOH to capture OH* and HMF* . As expected, the surface self-reconstructed $NiMo_3S_4$ ($NiMo_3S_4$-R: R means reconstruction) exhibits an extraordinary HMFOR activity with a small potential of 1.336 V (vs. reversible hydrogen electrode (RHE)) at 10 mA cm^{-2}. Furthermore, an HMF conversion of 99.3%, an FDCA selectivity of 98.7%, and a Faradaic efficiency of 98.5% were obtained by high-performance liquid chromatography (HPLC) analysis of oxidation products. Importantly, compared with contrast samples of NiS_2-R and Ni $(OH)_2$-R, $NiMo_3S_4$-R exhibited the stronger adsorption capability for C═O groups in HMF, indicating that the synergistic self-doping of Mo atoms and sulfate oxoanions into NiOOH not only modifies the electronic structure of Ni, but also adjusts the interaction between the electrocatalyst and the reactant while maintaining the structure of the precursor, which is vital to improve the catalytic activity and stability. Moreover, the $NiMo_3S_4$-R||$NiMo_3S_4$ electrolyzer for FDCA and H_2 production requires a low cell voltage of only 1.414 V to reach a current density of 10 mA cm^{-2}. This work sheds light on potential applications of surface-confined self-reconstruction and dual-activation strategies to design advanced electrocatalysts for biomass upgrading.

2. Experimental section

2.1. Chemicals

All chemical reagents were purchased without further purification. Nickel powder (Adamas, 99.95%), Molybdenum powder (Adamas, 99.99%), Sulfur powder (Adamas, 99.99%), Sodium Chloride (Adamas, 99.99%), Ethanol (Greagent, 99.7%), RuO_2 (Adamas, 99.95%), Pt/C (Sigma-Aldrich, 10 wt%), Nickel nitrate hexahydrate (Aladdin, 98%), Thiourea (Aladdin, 99%) KOH (Aladdin, 95%), 5-Hydroxymethyl-2-furaldehyde (Aladdin, 99%), and 2,5-Furandicarboxylic acid (Aladdin, 98%).

2.2. Synthesis of $NiMo_3S_4$

$NiMo_3S_4$ was synthesized via the high temperature molten salt method. Ni powder, Mo powder, S powder and NaCl powder were mixed together in the molar ratio of 1:3:4:100. Then they were ground thoroughly in a mortar. The mixed powders were pressed into a pellet and sealed in evacuated quartz tube, which were transferred into muffle furnace and annealed at 1000 °C for 24 h. After cooling to ambient temperature, the prepared precipitate was fully washed and dried.

2.3. Synthesis of Mo_3S_4

$NiMo_3S_4$ was etched in HCl (3 mol L^{-1}) for 30 min, and then the obtained sample were washed with deionized water and dried in a vacuum oven.

2.4. Synthesis of NiS_2

10 mmol of $Ni(NO_3)_2 0.6\ H_2O$, 10 mol of thiourea, and 6.25 mol of sulfur powder were dissolved in 80 mL of deionized water and then sonicated for 30 min before transferred to a Teflon-lined autoclave, which was heated to 200 °C for 24 h. After cooling to ambient temperature, the prepared precipitate was fully washed and dried. Afterwards, the samples were cooled down to room temperature naturally.

2.5. Materials characterization

X-ray diffraction (XRD) characterization was carried out by a Bruker D8 advance diffractometer operating with Cu Kα radiation. Transmission Electron Microscope (TEM) images were obtained by JEOL JEM-ARM300F. High resolution Cyro TEM images were obtained by Titan Krios G3 (D3500). The spherical aberration-corrected atomic resolution TEM images and EELS were obtained by Hitachi-HF5000. X-ray Photoelectron Spectroscopy (XPS) measurements were performed on a Thermo Scientific Escalab 250Xi. The X-ray absorption spectroscopy (XAS) data was acquired at bending magnet beamline 12-BM-B at the Advanced Photon Source (APS), Argonne National Laboratory. Raman spectra were obtained using a thermal dispersive spectrometer with laser excitation at 633 nm. Inductively Coupled Plasma Optical Emission Spectrometry (ICP-OES) results was obtained by Agilent 725-ES. The fourier transform infrared spectroscopy (FT-IR) was performed on Spotlight400.

2.6. TPD measurements

The measurements of HMF and CO TPD were carried out on an automatic gas-adsorption apparatus (BELCAT-A, BEL). Following temperature-programmed desorption in CO method. The sample was heated up to 423 K for 0.5 h at a rate of 10 K min^{-1} in He flow to remove adsorbed impurities. Then the sample was cooled down to 313 K for the adsorption of CO gas (99.999%). After flushing with He (99.999%) for 1 h to remove physically adsorbed CO, the TPD data were collected from 313 K to 773 K with a ramp of 10 K min^{-1} in the TCD detector. The pure

HMF was carried by He (99.999%) gas into catalysts until adsorption saturation and subsequently desorbed up to 473 K at He atmosphere.

2.7. Electrocatalytic measurement

The electrochemical experiments were carried out in a three-electrode cell using a CHI-760E electrochemical workstation at room temperature. The ink was prepared by dispersing 5 mg of the catalyst and 100 μL of 5 wt% Nafion solution in ethanol (900 μL) by sonication at least 30 min to form a homogeneous dispersion. Then, 100 μL of the dispersion was drop-casted onto a nickel foam (NF), leading to a catalyst loading of 2.5 mg cm^{-2}. During the electrochemical measurements, carbon rod and Hg/HgO electrode were used as the counter and reference electrodes, respectively. The KOH electrolyte was bubbled with N_2 and O_2 for 0.5 h before HER and OER test. The cyclic voltammogram (CV) was measured from 1.0 to 1.9 V vs. RHE for 50 cycles at a scan rate of 50 mV s^{-1} to form the activated layers. Polarization curves were recorded by linear sweep voltammetry (LSV) at a scan rate of 5 mV s^{-1} in the range of 1.0–1.8 V versus RHE for HMFOR and OER, 0.0 to − 0.7 V versus RHE for HER with iR compensation (95%). The overpotential (η) was calculated according to the formula: η = E (RHE) - 1.23 V. To estimate the electrochemically active surface area (ECSA) of the catalyst, cyclic voltammogram (CV) was tested by measuring double-layer capacitance (C_{dl}) between 1.10 and 1.30 V and between 0.0 and 0.2 V at various scan rates of 20–120 mV s^{-1} for HMFOR and HER, respectively. The in-situ Nyquist plots were measured with frequencies ranging from 100 kHz to 1 Hz, and the amplitude of 5 mV at a certain potential.

2.8. HPLC analysis

HPLC (Agilent1260) with an ultraviolet-visible detector was used to analyze HMF oxidation products. Specifically, 10 μL of electrolyte was sampling during potentiostatic electrolysis, which was diluted to 1 mL with ultrapure water and analyzed it by HPLC. The wavelength of the UV detector is set to 265 nm. The mobile phase A was methanol and phase B was acetonitrile with the A:B ratio 3:7. The flow rate is 0.6 mL min^{-1}. Using a 4.6 mm × 150 mm Shim-pack GWS 5 μm C18 column, each separation lasts 10 min. The HMF conversion, FDCA yield and faradaic efficiency were calculated using Eqs. (1)–(3), respectively.

HMF conversion (%) = [n (HMF consumed) / n (HMF initial)] × 100%　(1)

FDCA yield (%) = [n (FDCA formed) / n (HMF initial)] × 100%　　　(2)

Faradaic efficiency (%) = [n (FDCA formed) / (Charge / (6 × F))] × 100%(3)

where F is the Faraday constant (96,485 C mol^{-1}) and n is the mol of reactant calculated from the concentration measured by HPLC.

2.9. Density functional theory (DFT) calculations

All density functional theory (DFT) calculations were performed using the Vienna ab initio simulation package (VASP). In addition, the exchange-correlation functional was treated by the generalized gradient approximation with the Perdew−Burke−Ernzerh (GGA-PBE) functional. The supercell mode with 68 atoms for NiOOH nanosheet was built. The periodic surface was 12 Å × 12 Å with a vacuum slab of 25 Å in thickness to separate the layer from its periodic images. And the thickness of the slab is one layer. Considering the spin polarization, we set the parameter ISPIN to 2. The kinetic energy cut-off value was set to be 450 eV. A mesh of 3 × 3 × 1 was used for the k-point sampling obtained from the Gamma center. In geometry optimization, the atomic positions were fully optimized until the energy and forces were converged to 1 × 10^{-5} eV and 0.02 eV Å^{-1}, respectively. Finally, the adsorption energies (Eads) were calculated as E$_{*HMF}$=E$_{*/HMF}$-E$_*$-E$_{HMF}$, where E$_{*/HMF}$, E$_{HMF}$, and E$_*$ are the total energies of the optimized adsorbate/substrate system, the adsorbate in the gas phase, and the clean substrate, respectively. We also tested the stability of HMF in different positions and structures and selected the most stable configuration (Fig. S22).

3. Results and discussion

3.1. Electrocatalyst synthesis and reconstruction

The synthesis and subsequent surface-confined self-reconstruction processes of NiMo$_3$S$_4$ are illustrated in Fig. 1a. The NiMo$_3$S$_4$ sample was fabricated by the high-temperature molten salt method. And an ultra-thin (Ni, Mo)OOH layer with sulfate-terminated species was formed in situ on the surface of NiMo$_3$S$_4$ by electrochemical activation. The hypothesized surface structures for these samples after self-reconstruction (sample-R) are shown in Fig. 1b. Compared with pure NiOOH generated on Ni(OH)$_2$-R, the surface of NiS$_2$-R is NiOOH with sulfate oxoanions. Moreover, the surface of NiMo$_3$S$_4$-R is NiOOH modified by Mo dopants and sulfate oxoanions, leading to the charge redistribution of Ni sites, which can facilitate HMF adsorption and charge transfer [36,37]. Therefore, by combining the HMFOR and HER strategies, energy-saving and efficient hydrogen production with high-value-added products can be realized (Fig. 1c). The water is consumed at the cathode of NiMo$_3$S$_4$ to generate H$_2$ via HER, and the released OH$^-$ is transported to the anode side of NiMo$_3$S$_4$-R, facilitating the HMFOR, which has faster kinetics and yields more high-value-added FDCA than OER. As expected, NiMo$_3$S$_4$-R exhibits better HMFOR activity than NiS$_2$-R and Ni(OH)$_2$-R. Furthermore, compared with NiS$_2$ and Ni(OH)$_2$, NiMo$_3$S$_4$ shows enhanced HER performance, as shown in Fig. 1d.

The various CV curves (CV1-CV50) of NiMo$_3$S$_4$ activation in 1 M KOH are shown in Fig. 2a. The CV30 and CV50 curves are basically identical, indicating that surface self-reconstruction has been completed within the first 30 cycles and the oxidation/reduction peaks of the electrochemical activation CV correspond to Ni oxidation/reduction. In addition, the inductively coupled plasma optical emission spectroscopy (ICP–OES) results show that the concentration of molybdate and sulfate anions in the electrolyte increases with increasing CV cycles, and the concentration of molybdate and sulfate anions reaches a plateau after 30 cycles (Fig. S1). The X-ray diffraction (XRD) patterns of NiMo$_3$S$_4$, NiS$_2$, Ni(OH)$_2$, and Mo$_3$S$_4$ are shown in Figs. 2b and S2. The representative peaks of the as-prepared NiMo$_3$S$_4$ catalysts are consistent with the standard XRD pattern (JCPDS No. 30–0847), and the NiS$_2$, Ni(OH)$_2$, and Mo$_3$S$_4$ are also consistent with their standard XRD patterns. Moreover, the XRD pattern of NiMo$_3$S$_4$-R is approximately the same as that of NiMo$_3$S$_4$, which suggests that reconstruction occurs only on the surface and that the bulk NiMo$_3$S$_4$ structure is well maintained. The intensity of all the peaks becomes smaller due to the amorphous NiOOH thin layers on the surface of NiMo$_3$S$_4$, which affect the crystallinity degree of the material [38].

Transmission electron microscopy (TEM) images of NiMo$_3$S$_4$, NiS$_2$, Ni(OH)$_2$, and Mo$_3$S$_4$ are shown in Figs. 2c and S3, which display the nanoplate morphology of the as-prepared samples. In addition, the outer layer thickness of NiMo$_3$S$_4$ is thinner than that of NiS$_2$, Ni(OH)$_2$, and Mo$_3$S$_4$. The thinner outer layer of NiMo$_3$S$_4$ than that of compared catalysts, which is more facilitate to the activation process. The spherical aberration-corrected atomic resolution TEM image of NiMo$_3$S$_4$ is shown in the inset of Fig. 2c, showing lattice fringes of 0.32 nm attributed to the (002) planes of NiMo$_3$S$_4$. The high-angle annular dark-field scanning transmission electron microscopy (HAADF-STEM) images of NiMo$_3$S$_4$-R in Fig. 2d, e show that amorphous NiOOH coatings were formed in situ on the surface of the NiMo$_3$S$_4$ nanoplate is only ~5 nm due to the Mo dopants and sulfate oxoanions adsorption, and the interplanar spacing of 0.64 nm corresponds to the (001) plane of NiMo$_3$S$_4$. STEM energy-dispersive X-ray spectroscopy (EDS) elemental mapping reveals an amorphous NiOOH thin layer, as manifested by the presence of Ni and O, with a small amount of Mo and sulfate are modified on NiOOH, and the core of the NiMo$_3$S$_4$ nanoplate contains uniformly distributed Ni, Mo, and S (Fig. 2f). For comparison, the previous research reported that the
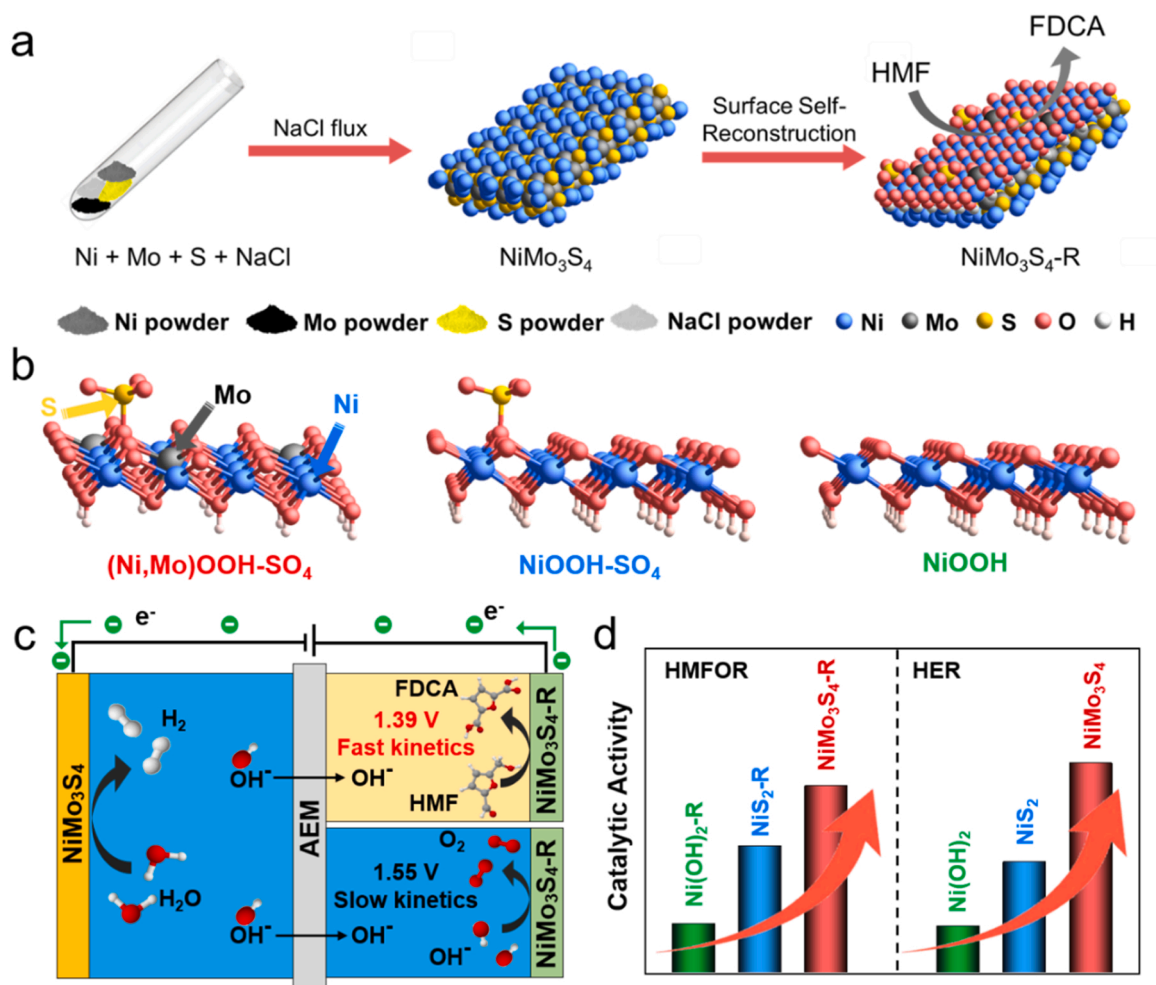
Fig. 1. Preparation of ultrathin (Ni, Mo)OOH layer with sulfate-terminated species via surface-confined self-reconstruction of $NiMo_3S_4$ for HMFOR. (a) Schematic illustration of synthesizing $NiMo_3S_4$ by solid state reaction and its subsequent surface reconstruction by CV activation in 1.0 M KOH. (b) Structural models of modified NiOOH ((Ni,Mo)OOH-SO_4 and NiOOH-SO_4) and pure NiOOH. NiOOH-SO_4 and NiOOH were prepared by electrochemical reconstruction of NiS_2 and Ni (OH)$_2$, respectively. (c) The advantages of HMFOR over OER for energy-saving and value-added feedstock production. (d) Activity comparison of $NiMo_3S_4$-R, NiS_2-R, and Ni(OH)$_2$-R for anodic HMFOR, and pristine $NiMo_3S_4$, NiS_2, and Ni(OH)$_2$ for cathodic HER.

thickness of reconstructed Ni(OH)$_2$ is exceed 20 nm and the crystalline NiS_2 transforms into an amorphous phase after 5 cycles but the $Fe_{0.1}Ni_{0.9}S_2$ only a few nm thick amorphous phase forms in the surface region [31,39].

Furthermore, Fig. 2g shows the high-resolution Cryo-TEM (Cryo-HRTEM) image of $NiMo_3S_4$-R, and Fig. 2h shows the electron energy-loss spectroscopy (EELS) maps with atomic resolution of the O K-edge and Ni L-edge. Notably, the integrated EELS signals of the Ni L-edge exist in both the outer region and core, and the signals of the O K-edge appearing in the outer region are significantly stronger, indicating the formation of ultrathin NiOOH layer on $NiMo_3S_4$. Furthermore, the significant differences in the EELS data (Fig. 2i) at O K-edge and Ni L-edge are that the external region (Fig. 2h, red region) has an obvious peak at 530 eV for the O K-edge and a Ni^{3+} peak at 870 eV for the Ni L-edge compared with interior region (Fig. 2h, blue region), which also proves the formation of NiOOH ultra-thin coating at the edge.

3.2. Electronic structure analysis

The details of specific surface elements and their redox states during the surface self-reconstruction of $NiMo_3S_4$ were further characterized by quasi-in situ X-ray photoelectron spectroscopy (XPS). For the high-resolution XPS of Ni 2p, two peaks assigned to Ni-S species at 852.4 and 869.7 eV gradually diminished from CV1 to CV5 because of surface

self-reconstruction (Fig. 3a). Moreover, two peaks at 855.5 (Ni-O) and 860.9 eV (Sat.) also shifted positively to higher binding energies during the surface self-reconstruction, demonstrating the high valency of Ni^{2+} oxidized to Ni^{3+} for the formation of Ni oxyhydroxide. The Mo 3d spectrum of $NiMo_3S_4$ can be deconvoluted into six subpeaks, corresponding to Mo^{3+} (228.1/231.5 eV), Mo^{4+} (228.9/233.4 eV), and Mo^{6+} (232.4/235.4 eV) of the Mo 3d$_{5/2}$ and Mo 3d$_{3/2}$ core levels, respectively (Fig. 3b). From CV1 to CV5, the contents of Mo^{3+} decrease with concomitant increases in Mo^{4+}, and from CV5 to CV50, the content of Mo^{6+} increases significantly, indicating the self-doping of Mo atoms. For the high-resolution XPS of S 2p (Fig. 3c), the peaks at 161.5 and 163.1 eV correspond to S 2p$_{3/2}$ and S 2p$_{1/2}$, respectively. A new peak attributed to $NiMo_3S_4$-R appeared at 168.9 eV, which is assigned to sulfate anions emerging from CV1 to CV10 and increasing significantly up to CV50.

X-ray absorption near-edge spectroscopy (XANES) and extended X-ray absorption fine structure (EXAFS) spectroscopy were conducted to assess the Ni electronic structure and coordination environments of $NiMo_3S_4$ during surface self-reconstruction (Fig. 3d-f). The white line intensity of $NiMo_3S_4$ in the Ni K-edge spectrum is between Ni foil and NiO, suggesting that the valence state of Ni in $NiMo_3S_4$ is between Ni^0 and Ni^{2+}. During the self-reconstruction process, the valence state of Ni follows the order of CV1 <CV10 <CV50, as manifested by the peak at ~8335 eV in the K-edge, demonstrating the change of average valence

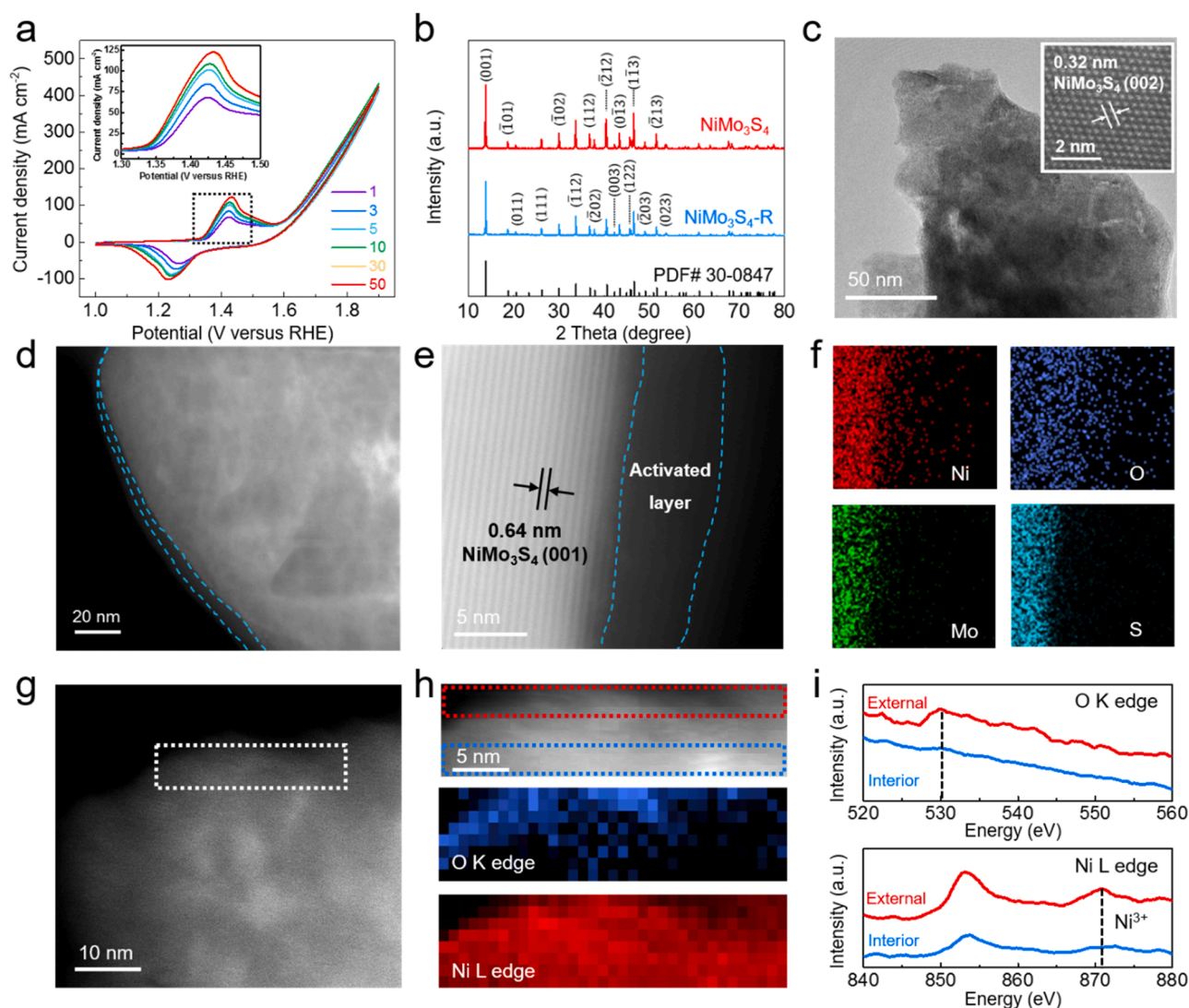**Fig. 2.** Structure and morphology characterizations of NiMo$_3$S$_4$-R. (a) CV curves of NiMo$_3$S$_4$ performed in a 1 M KOH solution for various cycles (from CV1 to CV50) at a scan rate of 5 mV s^{-1}. The inset shows the magnified CV curves. (b) XRD patterns of NiMo$_3$S$_4$ and NiMo$_3$S$_4$-R. (c) TEM and spherical aberration-corrected atomic resolution TEM image with fringe lattice spacing (inset) of NiMo$_3$S$_4$. (d) High-angle annular dark-field scanning transmission electron microscopy (HAADF-STEM) image of NiMo$_3$S$_4$-R. (e) Atomic-scale STEM image of NiMo$_3$S$_4$-R, showing an activated NiOOH layer on NiMo$_3$S$_4$-R. The matrix still maintains crystalline NiMo$_3$S$_4$. (f) The corresponding elemental mappings of Ni, Mo, S, and O in NiMo$_3$S$_4$-R. (g, h) High-resolution Cryo-TEM (Cryo-HRTEM) images and corresponding integrated EELS signal from the O K and Ni K-edges of NiMo$_3$S$_4$-R. (i) EELS spectra at the O K and Ni K ionization edges from corresponding regions, marked in (h).

in CV activation from Ni^{2+} to Ni^{3+} (Fig. 3d) [19]. As shown in the EXAFS spectra (Fig. 3e), a notable peak at approximately 2.0 Å was observed in the spectrum of NiMo$_3$S$_4$, corresponding to the Ni—O coordination. With an increase in the number of CV activation cycles, the main peaks associated with NiMo$_3$S$_4$ during surface self-reconstruction gradually shift from 2.0 Å to a shorter radial distance of 1.7 Å, suggesting Ni-O/Ni-S coordination, which indicates the formation of NiOOH [18].

The wavelet transformed (WT) Ni K-edge EXAFS oscillation of NiMo$_3$S$_4$ and various CV curves are given in Fig. 3f. Similarly, compared with the maximum intensity of the original NiMo$_3$S$_4$ (2.0 Å, Ni—S contribution), the gradual negative shift of the maximum intensity for CV1, CV10, and CV50 was due to the increasing contribution of Ni—O on the surface. To further confirm the formation of NiOOH, in situ Raman measurements were carried out to investigate the real-time changes of the NiMo$_3$S$_4$ catalyst during surface self-reconstruction. Fig. 3g shows the in-situ Raman spectra of NiMo$_3$S$_4$ at 0 V, which show three peaks at 236, 320, and 405 cm^{-1} assigned to Ni-S, Mo-S$_x$, and MoS$_2$, respectively. Importantly, the Raman spectra show two new peaks located at 477 and 554 cm^{-1}, corresponding to the Ni^{3+}-O

bending peak and Ni^{3+}-O stretching peak, respectively, thus demonstrating the generation of NiOOH [17,40]. Furthermore, the Raman mapping image also shows that the Raman intensity corresponding to NiOOH appeared to change at a voltage of 1.35 V and became stronger as the voltage increased (Fig. S4).

3.3. Electrocatalytic HMFOR and HER performance

The HMFOR (with 10 mM HMF) and OER (no HMF) of NiMo$_3$S$_4$-R, NiS$_2$-R, Ni(OH)$_2$-R, and Mo$_3$S$_4$-R were investigated by linear sweep voltammetry (LSV) in 1.0 M KOH, as shown in Fig. 4a. The OER of NiMo$_3$S$_4$-R had anode current densities of 10 and 100 mA cm^{-2} at 1.432 V and 1.550 V (vs. RHE), respectively. Moreover, in the presence of 10 mM HMF in the electrolyte, the oxidation potentials decreased to 1.336 V and 1.395 V (vs. RHE) at 10 and 100 mA cm^{-2}, respectively, indicating that the HMFOR is more energy saving than the OER. In addition, the various NiMo$_3$S$_4$-R (after CV30, after CV50, and after CV100) exhibits almost the same performance for HMFOR and OER as shown in Figs. S5 and S6, which consists with the CV results. The OER
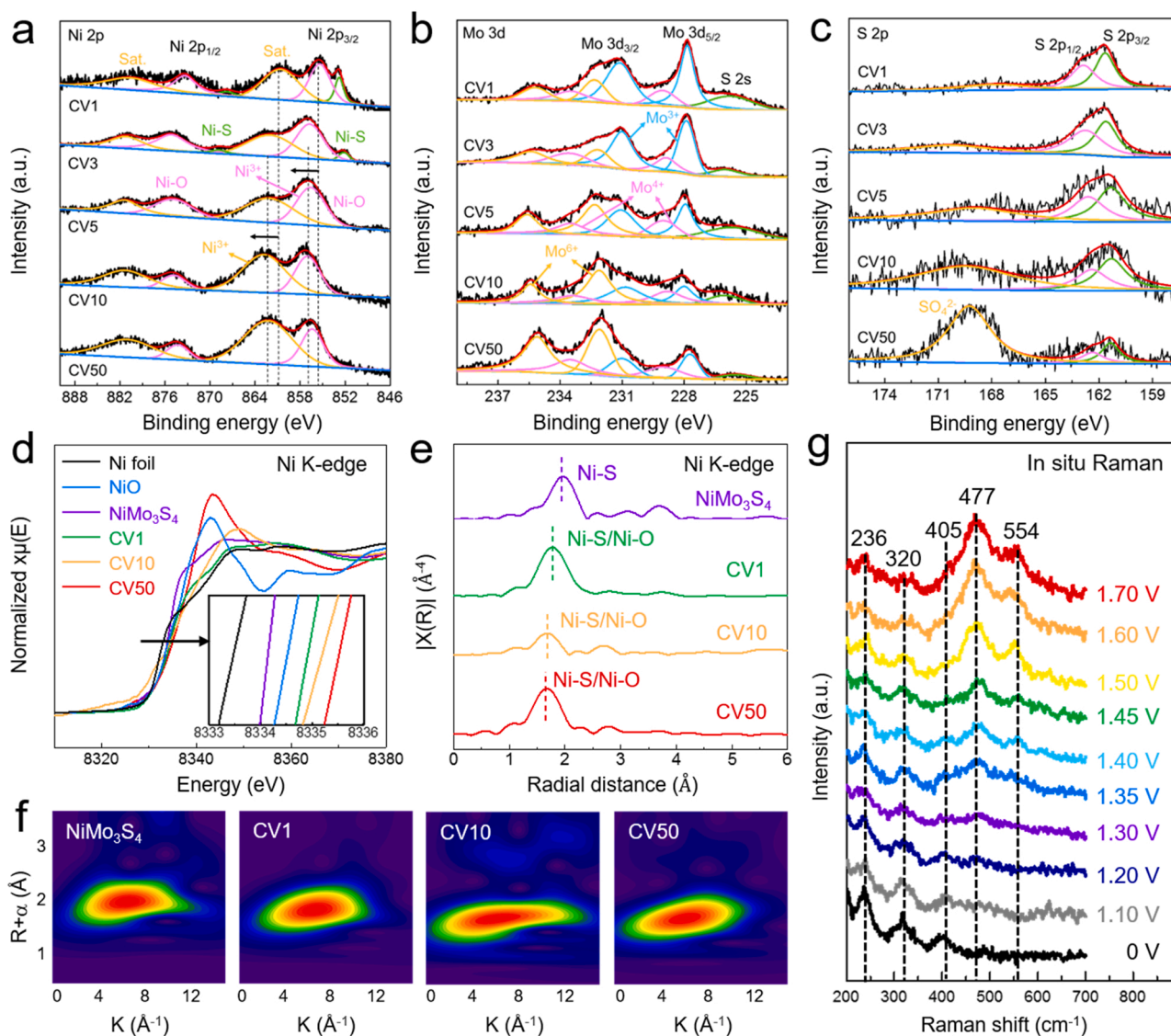
Fig. 3. Electronic structure analyses of $NiMo_3S_4$ and $NiMo_3S_4$-R. (a-c) High-resolution XPS of (a) Ni 2p, (b) Mo 3d, and (c) S 2p spectra of $NiMo_3S_4$ after various CV curves (CV1, CV3, CV5, CV10, and CV50) in 1 M KOH. (d) Normalized XANES spectra at the Ni K-edge, (e) EXAFS spectra in R-space at Ni K-edge for $NiMo_3S_4$, $NiMo_3S_4$ (CV1), $NiMo_3S_4$ (CV10), $NiMo_3S_4$ (CV50), Ni foil, and NiO samples. (f) Wavelet transforms for the k3-weighted Ni K-edge EXAFS of $NiMo_3S_4$, $NiMo_3S_4$ (CV1), $NiMo_3S_4$ (CV10), and $NiMo_3S_4$ (CV50). (g) In situ Raman spectra of $NiMo_3S_4$ at various potentials (from 0 V to 1.7 V) during OER process.

and HMFOR of NiS_2-R, $Ni(OH)_2$-R, and Mo_3S_4-R were also measured to realize the impact of NiOOH, Mo atoms, and sulfate oxoanions in $NiMo_3S_4$-R (Table S1). The performance of $NiMo_3S_4$-R was found to be superior to that of NiS_2-R, $Ni(OH)_2$-R, and Mo_3S_4-R, indicating that the formation of a Mo-atom and sulfate anion-modified NiOOH ultrathin coating is an efficient electrocatalyst of HMF oxidation. Moreover, the performance of $NiMo_3S_4$-R is also better than that of recently reported HMFOR electrocatalysts (Table S2) [11,15,16,41–46].

The Tafel slopes for HMFOR (Fig. S7) and OER (Fig. S8) of $NiMo_3S_4$-R were determined to be 36.5 and 80.7 mV dec^{-1}, which are smaller than those of NiS_2-R (120.4 and 194.1 mV dec^{-1}), $Ni(OH)_2$-R (191.7 and 216.1 mV dec^{-1}), and Mo_3S_4-R (240.3 and 237.7 mV dec^{-1}), indicating a faster electron-transfer rate. Exchange current density (j_0) can be obtained by the extrapolation method on the basis of the Tafel equation, which reflects the intrinsic activity of an electrocatalyst under equilibrium conditions (Fig. S9). The j_0 value of HMFOR for $NiMo_3S_4$-R is calculated to be 6.73×10^{-2} A cm^{-2}, which is higher than those of NiS_2-R (2.23×10^{-3} A cm^{-2}), $Ni(OH)_2$-R (1.19×10^{-3} A cm^{-2}), and Mo_3S_4-R (1.97×10^{-3} A cm^{-2}). This result indicates that a more than 30-fold increase in the exchange current density was observed. To provide

further insight into the catalytic performance, the j_0 of OER for $NiMo_3S_4$-R, NiS_2-R, $Ni(OH)_2$-R, and Mo_3S_4-R were also calculated, which is 3.06×10^{-2}, 2.13×10^{-3}, 2.85×10^{-3}, and 6.87×10^{-3} A cm^{-2}, respectively (Fig. S10).

By analyzing the in situ electrochemical impedance spectroscopy (EIS) of the HMFOR (Fig. S11) and OER (Fig. S12) for $NiMo_3S_4$-R, NiS_2-R, $Ni(OH)_2$-R, and Mo_3S_4-R at different potentials, the Nyquist plots of $NiMo_3S_4$-R showed an approximate vertical line at a low voltage of 1.05–1.20 V (vs. RHE), indicating a higher charge transfer resistance. When the applied voltage increased to 1.30 V (vs. RHE), an obvious mutation occurred in the Nyquist plots, indicating that HMF begins to oxidize. At the same time, the OER occurred at 1.45 V (vs. RHE), indicating that the reaction rate of HMF was significantly better than that of the OER, which is consistent with the LSV curve. Compared with NiS_2-R and $Ni(OH)_2$-R, the HMFOR and OER charge transfer resistance of $NiMo_3S_4$-R with ultrathin (Ni, Mo)OOH layer with sulfate-terminated species are significantly reduced. Furthermore, the electrochemically active surface area (ECSA) is an estimation of the active sites and can be calculated by the double-layer capacitance (C_{dl}) from their CV curves at the range of 1.1–1.3 V (Fig. S13). Notably, the C_{dl} value of 25.6 mF cm^{-2}
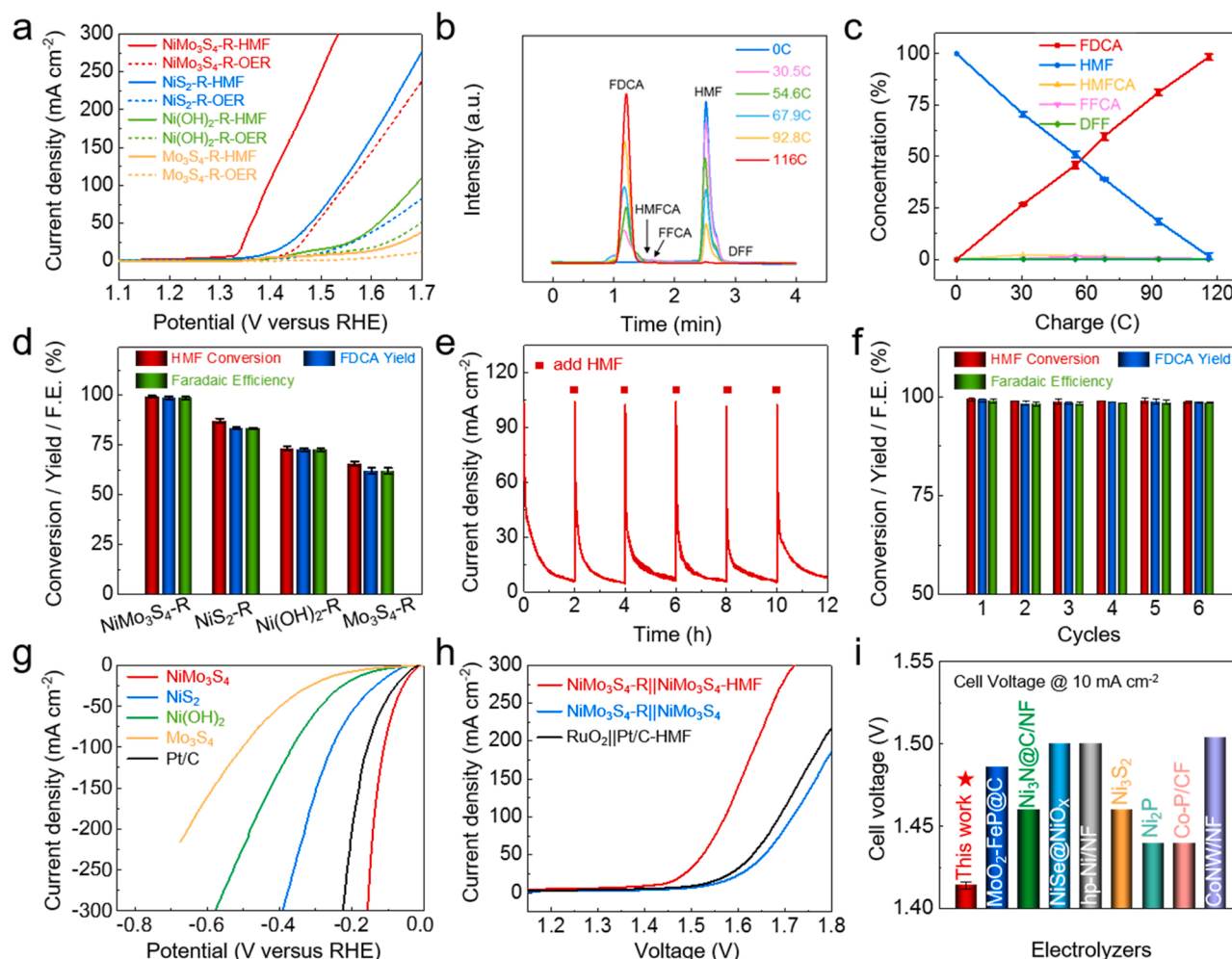
Fig. 4. Electrocatalytic performance of anodic HMFOR by NiMo$_3$S$_4$-R and cathodic HER by NiMo$_3$S$_4$. (a) Polarization curves of NiMo$_3$S$_4$-R, NiS$_2$-R, Ni(OH)$_2$-R, and Mo$_3$S$_4$-R in 1.0 M KOH with and without 10 mM HMF. (b) HPLC traces of HMF electrooxidation catalyzed by NiMo$_3$S$_4$-R in 20 mL 1.0 M KOH with 10 mM HMF. (c) Conversion changes of HMF and yields of products during the HMFOR process. (d) HMF conversion, FDCA selectivity, and Faradaic efficiency of NiMo$_3$S$_4$-R, NiS$_2$-R, Ni(OH)$_2$-R, and Mo$_3$S$_4$-R. (e, f) Chronoamperometry experiment and corresponding HMF conversion, FDCA selectivity, and Faradaic efficiency of NiMo$_3$S$_4$-R under six successive cycles of HMFOR. (g) Polarization curves of NiMo$_3$S$_4$, NiS$_2$, Ni(OH)$_2$, Mo$_3$S$_4$ and Pt/C for HER in 1.0 M KOH. (h) Polarization curves of NiMo$_3$S$_4$-R||NiMo$_3$S$_4$ with and without 10 mM HMF and RuO$_2$||Pt/C with 10 mM HMF in 1.0 M KOH. (i) Comparison of the electrolyzer voltages at 10 mA cm^{-2} for NiMo$_3$S$_4$-R||NiMo$_3$S$_4$ toward HMFOR||HER with recently reported electrocatalysts.

for NiMo$_3$S$_4$-R was obtained by evaluating the ECSA (Fig. S14), and this value is higher than those of NiS$_2$-R (19.0 mF cm^{-2}), Ni(OH)$_2$-R (18.1 mF cm^{-2}), and Mo$_3$S$_4$-R (13.3 mF cm^{-2}), indicating abundant active sites in NiMo$_3$S$_4$-R.

The NiMo$_3$S$_4$-R-catalyzed HMFOR was conducted in 20 mL of 1 M KOH with 10 mM HMF at an applied potential of 1.45 V (vs. RHE) to identify and quantify the oxidation products and calculate the corresponding Faradaic efficiencies. In theory, nearly 116 C is required to convert all the HMF into FDCA. As shown in Fig. 4b, the decrease in HMF and the concomitant increase in FDCA indicate the conversion of HMF to FDCA. When the amount of charge reaches 116 C, the peak of HMF almost disappears, while the peak of FDCA is maximal. Fig. 4c displays the conversion of HMF and the yield of the oxidation products as a function of charges consumed through the NiMo$_3$S$_4$ catalyst. There were two possible pathways for HMFOR, initial oxidization to 2,5-diformyl-furan (DFF) or 5-hydroxymethyl-2-furan-carboxylic acid (HMFCA) and then to 2-formyl-5-furancarboxylic acid (FFCA) to obtain HMFCA or DFF. Finally, FFCA is oxidized to FDCA (Fig. S15).
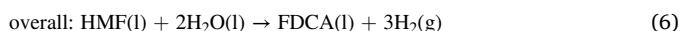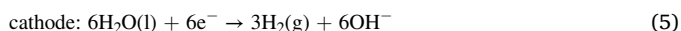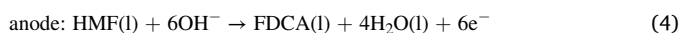
The product analysis showed that the yield of FDCA was close to 100%, while the yields of DFF, FFCA, and HMFCA were negligible. As shown in Fig. 4d, the HMF conversion, FDCA selectivity and Faradaic efficiency of NiMo$_3$S$_4$-R are 99.3%, 98.7% and 98.5%, respectively,

which are much higher than those of other catalysts NiS$_2$-R (87.1%, 83.5% and 83.3%), Ni(OH)$_2$-R (73.4%, 72.7% and 72.5%), and Mo$_3$S$_4$-R (65.6%, 62.1% and 61.9%). Furthermore, the stability of the NiMo$_3$S$_4$-R catalyst was ascertained by applying a constant potential of 1.45 V (vs. RHE) in 1.0 M KOH with 10 mM HMF for the HMFOR, and another aliquot of 10 mM HMF was added to the electrolyzer after the complete consumption of HMF (Fig. 4e). NiMo$_3$S$_4$-R exhibited an excellent electrochemical stability for the HMFOR and maintained a high FDCA yield, HMF conversion and FE after six continuous constant potential electrolysis cycles (Fig. 4f).

The electrocatalytic HER performance of NiMo$_3$S$_4$, NiS$_2$, Ni(OH)$_2$, and Mo$_3$S$_4$ was also evaluated in a 1.0 M KOH electrolyte (Fig. 4g). NiMo$_3$S$_4$ requires very low overpotentials of 36 and 111 mV at current densities of 10 and 100 mA cm^{-2}, respectively, which are lower than those required for Pt/C (48 and 157 mV), NiS$_2$ (89 and 256 mV), Ni (OH)$_2$ (159 and 366 mV), and Mo$_3$S$_4$ (227 and 503 mV) [47,48]. The LSV curve of NiMo$_3$S$_4$ after the addition of HMF was basically consistent with that without HMF, indicating that HMF has no effect on the HER (Fig. S16). Fig. S17 reveals that the lower Tafel slope, 28.8 mV dec^{-1}, was obtained for NiMo$_3$S$_4$ in comparison with those of NiS$_2$ (50.7 mV dec^{-1}), Ni(OH)$_2$ (135.1 mV dec^{-1}), and Mo$_3$S$_4$ (200.2 mV dec^{-1}). In addition, the performance of NiMo$_3$S$_4$ was better than those of most of

the recently reported Ni- or Mo-based HER electrocatalysts (Table S3) [19,49–57]. The C_{dl} of all samples was obtained by CV curves at the range of 0.0–0.2 V to evaluate the ECSA (Fig. S18). As shown in Fig. S19, the C_{dl} of NiMo$_3$S$_4$ was found to be 19.3 mF cm^{-2}, which is 1.69, 1.94, and 3.30 times those of NiS$_2$, Ni(OH)$_2$, and Mo$_3$S$_4$, suggesting the presence of more active sites in NiMo$_3$S$_4$.

To investigate the stability of NiMo$_3$S$_4$ for the HER, a long-term stability test was carried out (Fig. S20). The current density remained stable for 72 h, and the LSV curve of NiMo$_3$S$_4$ after testing basically overlapped with that of the original NiMo$_3$S$_4$, which indicates outstanding durability (Fig. S21). Inspired by the excellent catalytic performance of NiMo$_3$S$_4$-R and NiMo$_3$S$_4$, it was integrated into a two-electrode alkaline electrolyzer as an anode for the HMFOR and a cathode for the HER (Eqs. (1)–(3)). The high valence states of Ni^{3+} and Mo^{6+} in the NiMo$_3$S$_4$-R are conducive to the capture of OH$^-$ groups and obtain the electrons from HMF, which facilitating the HMFOR.

anode: $HMF(l) + 6OH^- \rightarrow FDCA(l) + 4H_2O(l) + 6e^-$　　　　　(4)

cathode: $6H_2O(l) + 6e^- \rightarrow 3H_2(g) + 6OH^-$　　　　　　　　(5)

overall: $HMF(l) + 2H_2O(l) \rightarrow FDCA(l) + 3H_2(g)$　　　　　(6)

For comparison, pure water splitting without HMF was also studied. The as-constructed NiMo$_3$S$_4$-R||NiMo$_3$S$_4$ electrolyzer displayed robust electrocatalytic properties (Fig. 4h), requiring low cell voltages of 1.414 V and 1.572 V to achieve 10 and 100 mA cm^{-2} in 1 M KOH with 10 mM HMF, much less than the cell voltages of commercial Pt/C||RuO$_2$ (1.511 V and 1.688 V) and overall water splitting without HMF (1.535 V and 1.717 V). Furthermore, compared with recently reported catalysts, the NiMo$_3$S$_4$-R||NiMo$_3$S$_4$ couples required the lower cell voltages to achieve current densities of 10 and 100 mA cm^{-2} (Fig. 4i and Table S4),

thus showing great promise of the NiMo$_3$S$_4$-R||NiMo$_3$S$_4$ paired electrolyzer for simultaneous H$_2$ production and HMF conversion [11,15,16, 43,44,58–60].

To better understand the electron transfer and reaction kinetics of NiMo$_3$S$_4$-R, NiS$_2$-R, Ni(OH)$_2$-R, and Mo$_3$S$_4$-R, in situ Bode phase plots at different potentials with and without HMF were prepared (Figs. 5a-c and S20). The peak in the low-frequency region is usually considered to correspond to the nonhomogeneous charge distribution caused by the formation of oxidation species on the electrode surface [15,61]. In the case of the electrolyte without HMF at potentials of 1.40 V, 1.50 V, and 1.55 V (vs. RHE), an obvious transition peak appeared for NiMo$_3$S$_4$-R, NiS$_2$-R, and Ni(OH)$_2$-R, respectively, indicating the emergence of oxygen evolution, which is consistent with the LSV curves for the OER. Moreover, the earlier transition peaks appeared for NiMo$_3$S$_4$-R, NiS$_2$-R, and Ni(OH)$_2$-R located at a potential of 1.30 V, 1.40 V, and 1.50 V, respectively (vs. RHE), in the electrolyte with HMF, demonstrating their higher reaction kinetics for the OER, which coincided with the LSV curves for the HMFOR. Additionally, the transition peak of Mo$_3$S$_4$-R appeared at 1.55 V in the electrolyte with or without HMF due to lack of NiOOH formation after surface reconstruction (Fig. S22).

3.4. Mechanism analysis of HMFOR

The reaction kinetics were impacted by the adsorption capacities of substrates and intermediates, so the adsorption behaviors of HMF on NiMo$_3$S$_4$-R, NiS$_2$-R, and Ni(OH)$_2$-R were examined by temperature-programmed desorption (TPD) measurements (Fig. 5d). The desorption temperature of NiMo$_3$S$_4$-R for HMF was found to be 124 °C, which is significantly higher than that of NiS$_2$-R (99 °C) and Ni(OH)$_2$-R (95 °C), demonstrating the stronger HMF adsorption energy of the
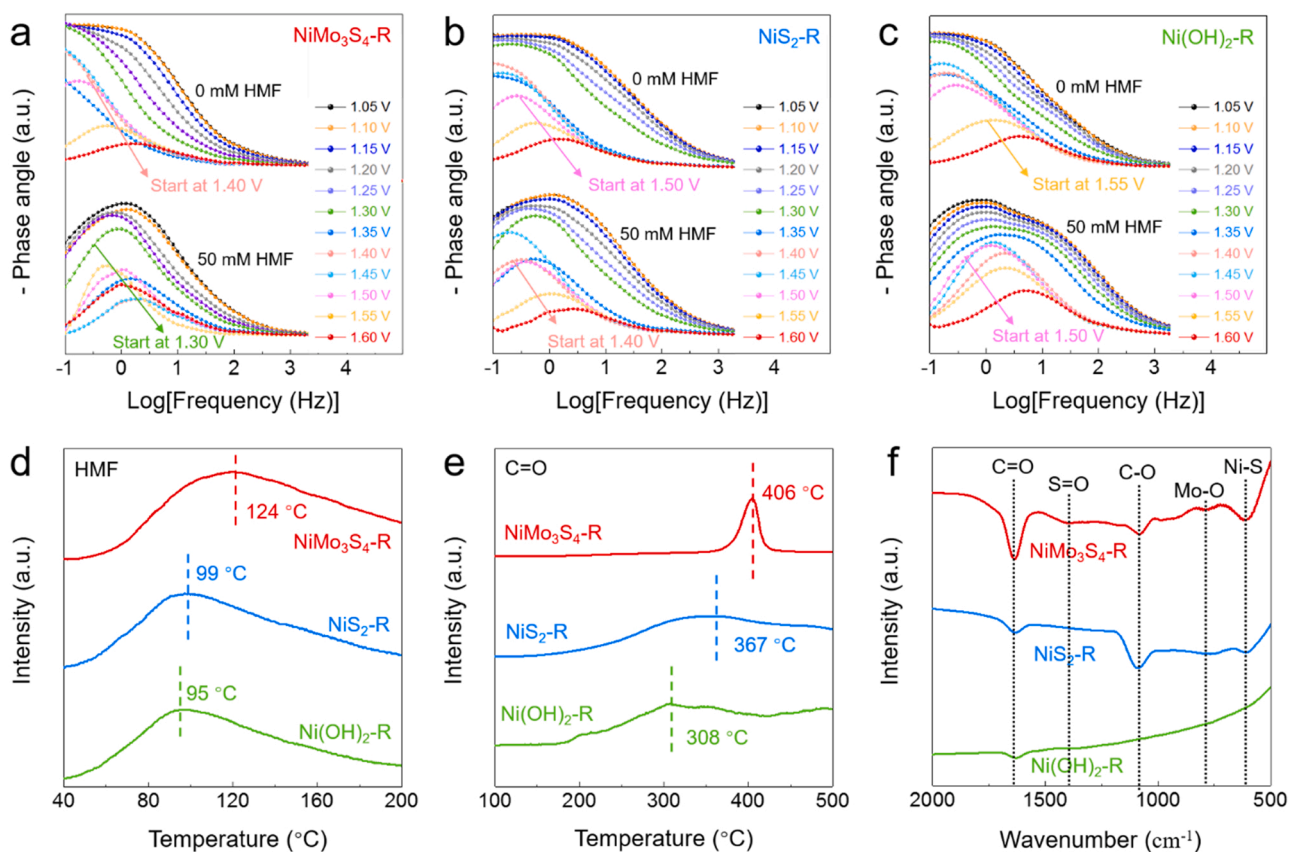

Fig. 5. HMFOR mechanism study of NiMo$_3$S$_4$-R. (a-c) Bode phase plots of the in situ electrochemical impedance spectroscopy of (a) NiMo$_3$S$_4$-R, (b) NiS$_2$-R, and (c) Ni(OH)$_2$-R with and without 50 mM HMF in 1 M KOH solution. (d, e) TPD spectra of NiMo$_3$S$_4$-R, NiS$_2$-R, and Ni(OH)$_2$-R under (d) HMF/He and (e) CO conditions. (f) FT-IR spectra of NiMo$_3$S$_4$-R, NiS$_2$-R, and Ni(OH)$_2$-R after adsorption of HMF.

ultrathin (Ni, Mo)OOH layer with sulfate-terminated species. In addition, TPD measurements were also carried out in a carbon monoxide atmosphere (C≡O) on NiMo$_3$S$_4$-R, NiS$_2$-R, and Ni(OH)$_2$-R to evaluate the preferred adsorption sites (Fig. 5e). In a carbon monoxide atmosphere, the desorption temperature of NiMo$_3$S$_4$-R (406 °C) was much higher than that of NiS$_2$-R (367 °C) and Ni(OH)$_2$-R (308 °C), indicating that NiMo$_3$S$_4$-R has a stronger adsorption energy for the C≡O group. To further validate the preferred adsorption of HMF, the FT-IR spectra of NiMo$_3$S$_4$-R, NiS$_2$-R, and Ni(OH)$_2$-R were obtained, as shown in Fig. 5f. The main peaks are located at 1663, 1409, 1065, 757, and 558 cm^{-1}, which were attributed to C≡O, S≡O, C—O, Mo—O, and Ni—S, respectively [62–64]. The TPD and FT-IR results indicate that the enhanced HMF adsorption should be attributed to the C≡O site rather than the C≡C site.

NiMo$_3$S$_4$ undergoes the surface-confined self-reconstruction to in situ generate NiOOH facilitated by synergistic activation with Mo atoms and sulfate oxoanions, which in turn leads to an enhanced electro-oxidation activity of HMF. To reveal the origin of the NiMo$_3$S$_4$-R-enhanced HMFOR, density functional theory (DFT) calculations were performed. Structural models of NiOOH modified by both Mo atoms and sulfate oxoanions, NiOOH modified by sulfate oxoanions, and pure NiOOH after HMF adsorption were established, corresponding to different chemical structures for the surface of NiMo$_3$S$_4$-R, NiS$_2$-R, and Ni(OH)$_2$-R, respectively (Figs. 6a, b, and S23). Our results show that the formyl groups of HMF are chemically adsorbed on the surface of NiOOH. As shown in Fig. 6c, the adsorption energies of HMF (E$_{*HMF}$) on NiMo$_3$S$_4$-R, NiS$_2$-R, and Ni(OH)$_2$-R were determined to be − 2.71 eV, − 1.48 eV, and − 1.01 eV, respectively, demonstrating the stronger interactions between HMF and NiOOH modified by both Mo atoms and sulfate oxoanions (Fig. 6a).

We also tested the stability of HMF in different positions and structures and selected the most stable configuration (Fig. S24). The charge density difference based on the above three models was calculated,

exhibiting charge transfer from the oxygen atoms of HMF to NiOOH (Fig. 6b). The number of electrons transferred (Δq) for NiMo$_3$S$_4$-R is 0.58 e, which is superior to those for NiS$_2$-R (0.42 e) and Ni(OH)$_2$-R (0.33 e). Moreover, compared with those of NiS$_2$-R and Ni(OH)$_2$-R, the adsorption energies of the OH groups (E$_{*OH}$) on NiMo$_3$S$_4$-R increased, which accelerates the HMFOR. The electron-localization function value at the junction of HMF and NiMo$_3$S$_4$-R was higher than that of NiS$_2$-R and Ni(OH)$_2$-R, further indicating the stronger interactions of this system (Fig. 6d). The density of states (DOS) of NiMo$_3$S$_4$-R is larger than those in the other two systems at the Fermi level, suggesting a high conductivity that could facilitate electron transfer during electro-catalysis (Fig. 6e). Therefore, the combined results of XPS, XANES, and DFT calculations, which indicating the Mo doping introduces an electronic redistribution in the Ni sites around the Mo sites.

4. Conclusion

In summary, we have demonstrated surface-confined self-reconstruction of NiMo$_3$S$_4$ into an amorphous NiOOH layer (NiMo$_3$S$_4$-R) modified by both Mo atoms and sulfate oxoanions via an electrochemical activation strategy, which shows excellent electrocatalytic activity for HMFOR. The in-situ formation of an ultrathin (Ni, Mo)OOH layer with sulfate-terminated species enhances the charge transfer and adsorption capacity of HMF and OH groups, thus significantly increasing the catalytic activity of HMFOR. As expected, NiMo$_3$S$_4$-R requires very low potentials of 1.336 V and 1.395 V (vs. RHE) to provide current densities of 10 and 100 mA cm^{-2}, respectively. The HMF conversion, FDCA selectivity, and Faradaic efficiency of NiMo$_3$S$_4$-R remain at 98.4%, 98.5%, and 98.4% after six continuous constant potential electrolysis cycles. Notably, a paired electrolyzer employing NiMo$_3$S$_4$-R for anodic HMFOR and NiMo$_3$S$_4$ for cathodic HER requires a very low voltage of 1.414 V and 1.572 V to reach 10 and 100 mA cm^{-2}, respectively, which is superior to those of most transition metal-based catalysts
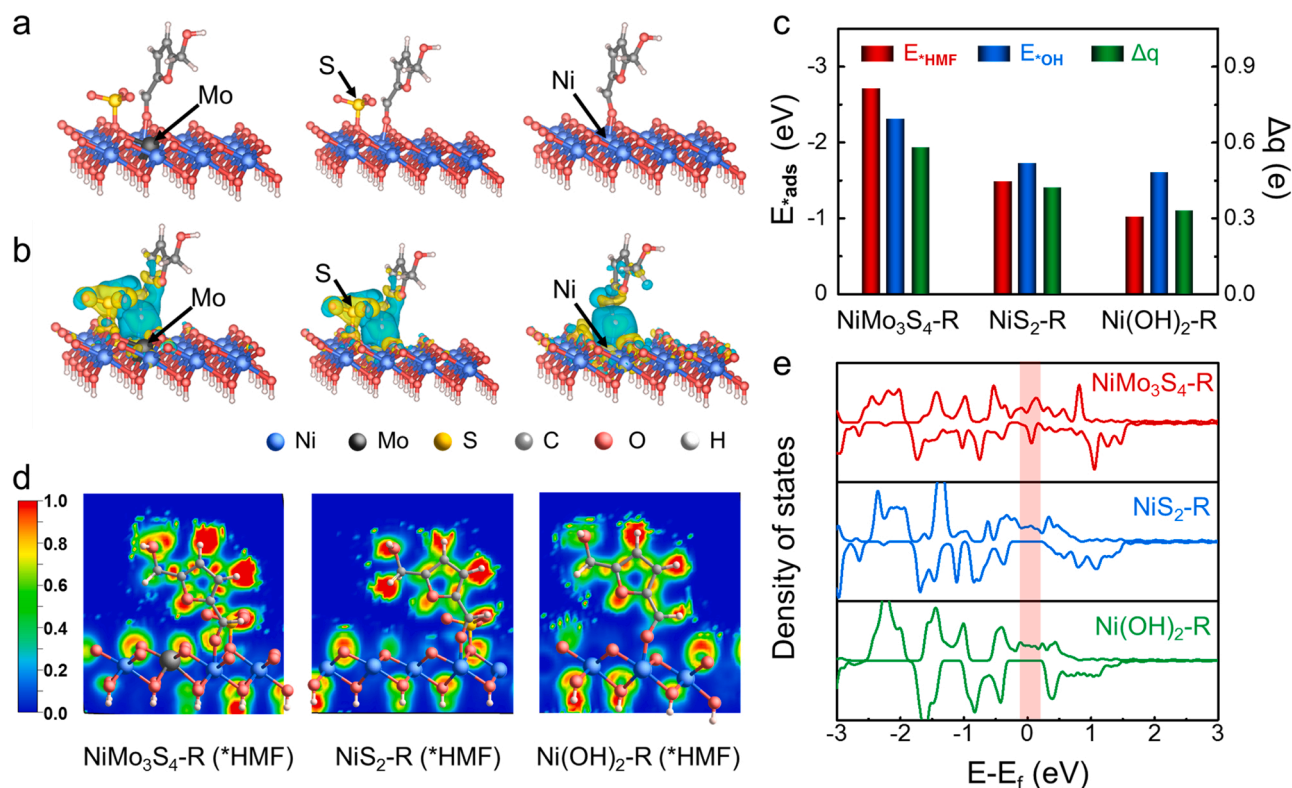

Fig. 6. DFT calculations. (a) Optimized structure models and (b) charge density difference of HMF adsorbed on NiMo$_3$S$_4$-R, NiS$_2$-R, and Ni(OH)$_2$-R. (c) Corresponding HMF adsorption energy, the number of electrons transferred, and OH adsorption energy of NiMo$_3$S$_4$-R, NiS$_2$-R, and Ni(OH)$_2$-R. (d) Electron localization function for the optimized HMF adsorption on NiMo$_3$S$_4$-R, NiS$_2$-R, and Ni(OH)$_2$-R. (e) Density of states on NiMo$_3$S$_4$-R, NiS$_2$-R, and Ni(OH)$_2$-R.

reported to date. This work provides a new avenue for the development of high-activity electrocatalysts through in situ surface-confined self-reconstruction for large-scale energy conversion applications.

CRediT authorship contribution statement

T.W. designed the experiments. T.W. and M.L. performed synthesis, characterization and catalytic reaction experiments. Z.X., Y.X., and H-L. W. provided the aberration-corrected TEM and Cryo-HRTEM characterizations. X.Z. and J.L. provided EXAFS measurements. X.W. and J.W. carried out DFT calculations. T.W., J.W., and F.H. performed the experimental data analysis. T.W. wrote the manuscript. J.L., J.W., H-L. W., and F.H. revised the manuscript. J.W., H-L.W., and F.H. supervised the project. All authors discussed the results and commented on the manuscript.

Declaration of Competing Interest

The authors declare that they have no known competing financial interests or personal relationships that could have appeared to influence the work reported in this paper.

Data availability

Data will be made available on request.

Acknowledgments

Appendix A. Supplementary material

Supplementary data associated with this article can be found in the online version at doi:10.1016/j.apcatb.2022.122126.

References

[1] Hydrogen on the rise, Nat. Energy, 1, 2016, p. 16127.
[2] W. Wang, Y.B. Zhu, Q. Wen, Y. Wang, J. Xia, C. Li, M.W. Chen, Y. Liu, H. Li, H. A. Wu, T. Zhai, Modulation of molecular spatial distribution and chemisorption with perforated nanosheets for ethanol electro-oxidation, Adv. Mater. 31 (2019), 1900528.
[3] E. Hayashi, Y. Yamaguchi, K. Kamata, N. Tsunoda, Y. Kumagai, F. Oba, M. Hara, Effect of MnO$_2$ crystal structure on aerobic oxidation of 5-hydroxymethylfurfural to 2,5-furandicarboxylic acid, J. Am. Chem. Soc. 141 (2019) 890–900.
[4] X. Lu, K.H. Wu, B. Zhang, J. Chen, F. Li, B.J. Su, P. Yan, J.M. Chen, W. Qi, Highly efficient electro-reforming of 5-Hydroxymethylfurfural on vertically oriented nickel nanosheet/carbon hybrid catalysts: structure-function relationships, Angew. Chem. Int. Ed. 60 (2021) 14528–14535.
[5] S. Rajendran, R. Raghunathan, I. Hevus, R. Krishnan, A. Ugrinov, M.P. Sibi, D. C. Webster, J. Sivaguru, Programmed photodegradation of polymeric/oligomeric materials derived from renewable bioresources, Angew. Chem. Int. Ed. 54 (2015) 1159–1163.
[6] B. You, Y. Sun, Innovative strategies for electrocatalytic water splitting, Acc. Chem. Res. 51 (2018) 1571–1580.
[7] J. Kiwi, M. Gratzel, Oxygen evolution from water via redox catalysis, Angew. Chem. Int. Ed. 17 (1978) 860–861.
[8] O. Kasian, J.P. Grote, S. Geiger, S. Cherevko, K.J. Mayrhofer, The common intermediates of oxygen evolution and dissolution reactions during water electrolysis on iridium, Angew. Chem. Int. Ed. 57 (2018) 2488–2491.
[9] J. Li, R. Güttinger, R. Moré, F. Song, W. Wan, G.R. Patzke, Frontiers of water oxidation: the quest for true catalysts, Chem. Soc. Rev. 46 (2017) 6124–6147.
[10] Y. Ping, R.J. Nielsen, W.A. Goddard III, The reaction mechanism with free energy barriers at constant potentials for the oxygen evolution reaction at the IrO$_2$ (110) surface, J. Am. Chem. Soc. 139 (2016) 149–155.
[11] G. Yang, Y. Jiao, H. Yan, Y. Xie, A. Wu, X. Dong, D. Guo, C. Tian, H. Fu, Interfacial engineering of MoO$_2$-FeP heterojunction for highly efficient hydrogen evolution coupled with biomass electrooxidation, Adv. Mater. 32 (2020), 2000455.
[12] Y. Lu, C.L. Dong, Y.C. Huang, Y. Zou, Z. Liu, Y. Liu, Y. Li, N. He, J. Shi, S. Wang, Identifying the geometric site dependence of spinel oxides for the electrooxidation of 5-hydroxymethylfurfural, Angew. Chem. Int. Ed. 59 (2020) 19215–19221.
[13] K. Gu, D. Wang, C. Xie, T. Wang, G. Huang, Y. Liu, Y. Zou, L. Tao, S. Wang, Defect-rich high-entropy oxide nanosheets for efficient 5-hydroxymethylfurfural electrooxidation, Angew. Chem. Int. Ed. 60 (2021) 20253–20258.
[14] P. Zhang, X. Sheng, X. Chen, Z. Fang, J. Jiang, M. Wang, F. Li, L. Fan, Y. Ren, B. Zhang, B.J.J. Timmer, M.S.G. Ahlquist, L. Sun, Paired electrocatalytic oxygenation and hydrogenation of organic substrates with water as the oxygen and hydrogen source, Angew. Chem. Int. Ed. 58 (2019) 9155–9159.
[15] N. Zhang, Y. Zou, L. Tao, W. Chen, L. Zhou, Z. Liu, B. Zhou, G. Huang, H. Lin, S. Wang, Electrochemical oxidation of 5-hydroxymethylfurfural on nickel nitride/carbon nanosheets: reaction pathway determined by in situ sum frequency generation vibrational spectroscopy, Angew. Chem. Int. Ed. 58 (2019) 15895–15903.
[16] B. You, X. Liu, N. Jiang, Y. Sun, A general strategy for decoupled hydrogen production from water splitting by integrating oxidative biomass valorization, J. Am. Chem. Soc. 138 (2016) 13639–13646.
[17] L. Yu, Q. Zhu, S. Song, B. McElhenny, D. Wang, C. Wu, Z. Qin, J. Bao, Y. Yu, S. Chen, Non-noble metal-nitride based electrocatalysts for high-performance alkaline seawater electrolysis, Nat. Commun. 10 (2019) 5106.
[18] X. Ren, C. Wei, Y. Sun, X. Liu, F. Meng, X. Meng, S. Sun, S. Xi, Y. Du, Z. Bi, G. Shang, A.C. Fisher, L. Gu, Z.J. Xu, Constructing an adaptive heterojunction as a highly active catalyst for the oxygen evolution reaction, Adv. Mater. 32 (2020), 2001292.
[19] H. Sun, L. Chen, Y. Lian, W. Yang, L. Lin, Y. Chen, J. Xu, D. Wang, X. Yang, M. H. Rummerli, J. Guo, J. Zhong, Z. Deng, Y. Jiao, Y. Peng, S. Qiao, Topotactically transformed polygonal mesopores on ternary layered double hydroxides exposing under-coordinated metal centers for accelerated water dissociation, Adv. Mater. 32 (2020), 2006784.
[20] S. Chen, J. Duan, J. Ran, M. Jaroniec, S.Z. Qiao, N-doped graphene film-confined nickel nanoparticles as a highly efficient three-dimensional oxygen evolution electrocatalyst, Energy Environ. Sci. 6 (2013) 3693.
[21] S. Li, Z. Li, R. Ma, C. Gao, L. Liu, L. Hu, J. Zhu, T. Sun, Y. Tang, D. Liu, J. Wang, A glass-ceramic with accelerated surface reconstruction toward the efficient oxygen evolution reaction, Angew. Chem. Int. Ed. 60 (2021) 3773–3780.
[22] B. Wang, C. Tang, H.F. Wang, B.Q. Li, X. Cui, Q. Zhang, Anion-regulated hydroxysulfide monoliths as OER/ORR/HER electrocatalysts and their applications in self-powered electrochemical water splitting, Small Methods 2 (2018), 1800055.
[23] P. Chen, T. Zhou, S. Wang, N. Zhang, Y. Tong, H. Ju, W. Chu, C. Wu, Y. Xie, Dynamic migration of surface fluorine anions on cobalt-based materials to achieve enhanced oxygen evolution catalysis, Angew. Chem. Int. Ed. 57 (2018) 15471–15475.
[24] N. Han, F. Zhao, Y. Li, Ultrathin nickel–iron layered double hydroxide nanosheets intercalated with molybdate anions for electrocatalytic water oxidation, J. Mater. Chem. A 3 (2015) 16348–16353.
[25] Y. Sun, R. Li, X. Chen, J. Wu, Y. Xie, X. Wang, K. Ma, L. Wang, Z. Zhang, Q. Liao, Z. Kang, Y. Zhang, A-site management prompts the dynamic reconstructed active phase of perovskite oxide OER catalysts, Adv. Energy Mater. 11 (2021), 2003755.
[26] B. Wang, K. Zhao, Z. Yu, C. Sun, Z. Wang, N. Feng, L. Mai, Y. Wang, Y. Xia, In situ structural evolution of the multi-site alloy electrocatalyst to manipulate the intermediate for enhanced water oxidation reaction, Energy Environ. Sci. 13 (2020) 2200–2208.
[27] B. Jiang, Z. Wan, Y. Kang, Y. Guo, J. Henzie, J. Na, H. Li, S. Wang, Y. Bando, Y. Sakka, Y. Yamauchi, Auto-programmed synthesis of metallic aerogels: Core-shell Cu@Fe@Ni aerogels for efficient oxygen evolution reaction, Nano Energy 81 (2021), 105644.
[28] J. Huang, Y. Li, Y. Zhang, G. Rao, C. Wu, Y. Hu, X. Wang, R. Lu, Y. Li, J. Xiong, Identification of key reversible intermediates in self-reconstructed nickel-based hybrid electrocatalysts for oxygen evolution, Angew. Chem. Int. Ed. 131 (2019) 17619–17625.
[29] X. Liu, J. Meng, K. Ni, R. Guo, F. Xia, J. Xie, X. Li, B. Wen, P. Wu, M. Li, Complete reconstruction of hydrate pre-catalysts for ultrastable water electrolysis in industrial-concentration alkali media, Cell Rep. Phys. Sci. 1 (2020), 100241.
[30] M. Cui, X. Bai, J. Zhu, C. Han, Y. Huang, L. Kang, C. Zhi, H. Li, Electrochemically induced NiCoSe$_2$@NiOOH/CoOOH heterostructures as multifunctional cathode materials for flexible hybrid zn batteries, Energy Storage Mater. 36 (2021) 427–434.
[31] N. Clament Sagaya Selvam, S.J. Kwak, G.H. Choi, M.J. Oh, H. Kim, W.-S. Yoon, W. B. Lee, P.J. Yoo, Unveiling the impact of Fe incorporation on intrinsic performance of reconstructed water oxidation electrocatalyst, ACS Energy Lett. 6 (2021) 4345–4354.
[32] R.T. Gao, D. He, L. Wu, K. Hu, X. Liu, Y. Su, L. Wang, Towards long-term photostability of nickel hydroxide/BiVO$_4$ photoanodes for oxygen evolution catalysts via in situ catalyst tuning, Angew. Chem. Int. Ed. 59 (2020) 6213–6218.
[33] K. Wang, H. Du, S. He, L. Liu, K. Yang, J. Sun, Y. Liu, Z. Du, L. Xie, W. Ai, W. Huang, Kinetically controlled, scalable synthesis of γ-FeOOH nanosheet arrays on nickel foam toward efficient oxygen evolution: the key role of in-situ-generated γ-NiOOH, Adv. Mater. 33 (2021), 2005587.
[34] J. Bai, J. Mei, T. Liao, Q. Sun, Z.G. Chen, Z. Sun, Molybdenum-promoted surface reconstruction in polymorphic cobalt for initiating rapid oxygen evolution, Adv. Energy Mater. 12 (2022), 2103247.
[35] Y. Chen, Z. Lai, X. Zhang, Z. Fan, Q. He, C. Tan, H. Zhang, Phase engineering of nanomaterials, Nat. Rev. Chem. 4 (2020) 243–256.
[36] H. Huang, D. Yu, F. Hu, S.C. Huang, J. Song, H.Y. Chen, L.L. Li, S. Peng, Clusters induced electron redistribution to tune oxygen reduction activity of transition metal single-atom for metal–air batteries, Angew. Chem. Int. Ed. 134 (2022), e202116068.

[37] J. Song, S. Qiu, F. Hu, Y. Ding, S. Han, L. Li, H.Y. Chen, X. Han, C. Sun, S. Peng, Sub-2 nm thiophosphate nanosheets with heteroatom doping for enhanced oxygen electrocatalysis, Adv. Funct. Mater. 31 (2021), 2100618.

[38] B. Zhang, K. Jiang, H. Wang, S. Hu, Fluoride-induced dynamic surface self-reconstruction produces unexpectedly efficient oxygen-evolution catalyst, Nano Lett. 19 (2018) 530–537.

[39] X. Ding, W. Li, H. Kuang, M. Qu, M. Cui, C. Zhao, D.-C. Qi, F.E. Oropeza, K. H. Zhang, An Fe stabilized metallic phase of NiS2 for the highly efficient oxygen evolution reaction, Nanoscale 11 (2019) 23217–23225.

[40] T. Wu, E. Song, S. Zhang, M. Luo, C. Zhao, W. Zhao, J. Liu, F. Huang, Engineering metallic heterostructure based on Ni3N and 2M-MoS2 for alkaline water electrolysis with industry-compatible current density and stability, Adv. Mater. 34 (2022), 2108505.

[41] S. Barwe, J. Weidner, S. Cychy, D.M. Morales, S. Dieckhöfer, D. Hiltrop, J. Masa, M. Muhler, W. Schuhmann, Electrocatalytic oxidation of 5-(hydroxymethyl) furfural using high-surface-area nickel boride, Angew. Chem. Int. Ed. 57 (2018) 11460–11464.

[42] S. Li, X. Sun, Z. Yao, X. Zhong, Y. Cao, Y. Liang, Z. Wei, S. Deng, G. Zhuang, X. Li, J. Wang, Biomass valorization via paired electrosynthesis over vanadium nitride-based electrocatalysts, Adv. Funct. Mater. 29 (2019), 1904780.

[43] N. Jiang, B. You, R. Boonstra, I.M. Terrero Rodriguez, Y. Sun, Integrating electrocatalytic 5-hydroxymethylfurfural oxidation and hydrogen production via Co–P-derived electrocatalysts, ACS Energy Lett. 1 (2016) 386–390.

[44] B. You, X. Liu, X. Liu, Y. Sun, Efficient H2 evolution coupled with oxidative refining of alcohols via a hierarchically porous nickel bifunctional electrocatalyst, ACS Catal. 7 (2017) 4564–4570.

[45] L. Wang, J. Cao, C. Lei, Q. Dai, B. Yang, Z. Li, X. Zhang, C. Yuan, L. Lei, Y. Hou, Strongly coupled 3D N-Doped MoO2/Ni3S2 hybrid for high current density hydrogen evolution electrocatalysis and biomass upgrading, ACS Appl. Mater. Interfaces 11 (2019) 27743–27750.

[46] M. Zhang, Y. Liu, B. Liu, Z. Chen, H. Xu, K. Yan, Trimetallic NiCoFe-layered double hydroxides nanosheets efficient for oxygen evolution and highly selective oxidation of biomass-derived 5-hydroxymethylfurfural, ACS Catal. 10 (2020) 5179–5189.

[47] L. Li, D. Yu, P. Li, H. Huang, D. Xie, C.-C. Lin, F. Hu, H.-Y. Chen, S. Peng, Interfacial electronic coupling of ultrathin transition-metal hydroxide nanosheets with layered MXenes as a new prototype for platinum-like hydrogen evolution, Energ. Environ. Sci. 14 (2021) 6419–6427.

[48] L. Deng, F. Hu, M. Ma, S.C. Huang, Y. Xiong, H.Y. Chen, L. Li, S. Peng, Electronic modulation caused by interfacial Ni-O-M (M= Ru, Ir, Pd) bonding for accelerating hydrogen evolution kinetics, Angew. Chem. Int. Ed. 133 (2021) 22450–22456.

[49] J. Zhang, T. Wang, P. Liu, S. Liu, R. Dong, X. Zhuang, M. Chen, X. Feng, Engineering water dissociation sites in MoS2 nanosheets for accelerated electrocatalytic hydrogen production, Energ. Environ. Sci. 9 (2016) 2789–2793.

[50] Y. Wu, F. Li, W. Chen, Q. Xiang, Y. Ma, H. Zhu, P. Tao, C. Song, W. Shang, T. Deng, Coupling interface constructions of MoS2/Fe5Ni4S8 heterostructures for efficient electrochemical water splitting, Adv. Mater. 30 (2018), 1803151.

[51] H. Li, S. Chen, Y. Zhang, Q. Zhang, X. Jia, Q. Zhang, L. Gu, X. Sun, L. Song, X. Wang, Systematic design of superaerophobic nanotube-array electrode comprised of transition-metal sulfides for overall water splitting, Nat. Commun. 9 (2018) 2452.

[52] C. Lei, Y. Wang, Y. Hou, P. Liu, J. Yang, T. Zhang, X. Zhuang, M. Chen, B. Yang, L. Lei, C. Yuan, M. Qiu, X. Feng, Efficient alkaline hydrogen evolution on atomically dispersed Ni–Nx Species anchored porous carbon with embedded Ni nanoparticles by accelerating water dissociation kinetics, Energy Environ. Sci. 12 (2019) 149–156.

[53] Y. Zang, S. Niu, Y. Wu, X. Zheng, J. Cai, J. Ye, Y. Xie, Y. Liu, J. Zhou, J. Zhu, X. Liu, G. Wang, Y. Qian, Tuning orbital orientation endows molybdenum disulfide with exceptional alkaline hydrogen evolution capability, Nat. Commun. 10 (2019) 1217.

[54] P. Zhai, Y. Zhang, Y. Wu, J. Gao, B. Zhang, S. Cao, Y. Zhang, Z. Li, L. Sun, J. Hou, Engineering active sites on hierarchical transition bimetal oxides/sulfides heterostructure array enabling robust overall water splitting, Nat. Commun. 11 (2020) 5462.

[55] H. Li, S. Chen, X. Jia, B. Xu, H. Lin, H. Yang, L. Song, X. Wang, Amorphous nickel-cobalt complexes hybridized with 1T-phase molybdenum disulfide via hydrazine-induced phase transformation for water splitting, Nat. Commun. 8 (2017) 15377.

[56] X. Li, Y. Wang, J. Wang, Y. Da, J. Zhang, L. Li, C. Zhong, Y. Deng, X. Han, W. Hu, Sequential electrodeposition of bifunctional catalytically active structures in MoO3/Ni–NiO composite electrocatalysts for selective hydrogen and oxygen evolution, Adv. Mater. 32 (2020), 2003414.

[57] Y. Yang, H. Yao, Z. Yu, S.M. Islam, H. He, M. Yuan, Y. Yue, K. Xu, W. Hao, G. Sun, Hierarchical nanoassembly of MoS2/Co9S8/Ni3S2/Ni as a highly efficient electrocatalyst for overall water splitting in a wide pH range, J. Am. Chem. Soc. 141 (2019) 10417–10430.

[58] L. Gao, Z. Liu, J. Ma, L. Zhong, Z. Song, J. Xu, S. Gan, D. Han, L. Niu, NiSe@NiOx core-shell nanowires as a non-precious electrocatalyst for upgrading 5-hydroxy-methylfurfural into 2,5-furandicarboxylic acid, Appl. Catal. B Environ. 261 (2020), 118235.

[59] B. You, N. Jiang, X. Liu, Y. Sun, Simultaneous H2generation and biomass upgrading in water by an efficient noble-metal-free bifunctional electrocatalyst, Angew. Chem. Int. Ed. 55 (2016) 9913–9917.

[60] Z. Zhou, C. Chen, M. Gao, B. Xia, J. Zhang, In situ anchoring of a Co3O4 nanowire on nickel foam: an outstanding bifunctional catalyst for energy-saving simultaneous reactions, Green Chem. 21 (2019) 6699–6706.

[61] Y. Lu, C.L. Dong, Y.C. Huang, Y. Zou, Z. Liu, Y. Liu, Y. Li, N. He, J. Shi, S. Wang, Identifying the geometric site dependence of spinel oxides for the electrooxidation of 5–hydroxymethylfurfural, Angew. Chem. Int. Ed. 59 (2020) 19215–19221.

[62] J. Vijayakumari, T.L. Stephan Raj, Analysis of bioactive compounds in Dicranopteris linearis (Burm.F.) Underw, J. Pharm. Sci. Innov. 8 (2019) 136–140.

[63] X. Yang, Y. Zhao, R. Li, Y. Wu, M. Yang, A modified kinetic analysis method of cellulose pyrolysis based on TG–FTIR technique, Thermochim. Acta 665 (2018) 20–27.

[64] P.-F. Yin, C. Zhou, X.-Y. Han, Z.-R. Zhang, C.-H. Xia, L.-L. Sun, Shape and phase evolution of nickel sulfide nano/microcrystallines via a facile way, J. Alloy. Compd. 620 (2015) 42–47.